ARCHIVE OF MECHANICAL ENGINEERING

DOI: 10.24425/ame.2025.154740

2025, Vol. 72, No. 3, pp. 379-403

Ferenc KUBICSEK D 1, Ferenc HEGEDŰS D 1, Péter CSIZMADIA D 1

Optimization of sonochemical ammonia synthesis in non-Newtonian fluids

Received 18 April 2025, Revised 6 June 2025, Accepted 3 July 2025, Published online 21 July 2025

Keywords: ammonia, Haber–Bosch process, energy intensity, sonochemistry, microbubbles

This study investigates the theoretical energy intensity of ammonia production via sonochemical reactions in non-Newtonian test fluids. A single, freely oscillating microbubble containing nitrogen and hydrogen is modelled using the Keller–Miksis equation, the first law of thermodynamics, and a detailed reaction mechanism. The goal is to assess whether modifying fluid properties can improve the energy intensity compared to conventional methods. Key parameters—including bubble size, ambient pressure, gas composition, and rheological properties—are varied systematically. The total energy input includes bubble expansion work, hydrogen production via electrolysis, and gas compression energy. The lowest energy intensity achieved is 682.6 GJ/t, which is 17.5 times higher than the Haber–Bosch process using renewable hydrogen. Compared to previous studies in water, a 5.3% improvement is observed, attributed primarily to the increased sound speed. The non-Newtonian rheology had only minor influence, suggesting that future efforts should focus on optimizing acoustic parameters and fluid compressibility rather than rheological properties.

1. Introduction

Currently ammonia plays a crucial role in the global economy. In the modern agriculture, 70% of the produced ammonia is used to produce nitrogen fertilizers as a primary commodity [1]. Furthermore, ammonia is also an energy carrier: it can be used as a fuel as well [2, 3]. It implies that in the forthcoming decades, ammonia demand is expected to have a significant growth, from 180 million tons (Mt) to 668 Mt by 2050 [4]. Nowadays, ammonia is produced mainly by the

¹Department of Hydrodynamic Systems, Faculty of Mechanical Engineering, Budapest University of Technology and Economics, Budapest, Hungary. Emails: fkubicsek@hds.bme.hu, fhegedus@hds.bme.hu, pcsizmadia@hds.bme.hu



[☑] Ferenc KUBICSEK, email: fkubicsek@hds.bme.hu



more than a century-old Haber–Bosch process, in which nitrogen and hydrogen are reacted catalytically under high temperature (500 °C) and pressure (400 bar). The process is very difficult and has a large energy demand: using the best available technology (BAT), where the hydrogen source is methane, the energy intensity of the Haber–Bosch process is 28 GJ/t [1]. The hydrogen can be produced from water electrolysis using renewable electricity as well, which is an environmentally more friendly method, nevertheless, in this case, the energy intensity of the process is substantially higher: 39.1 GJ/t [5]. The nitrogen is obtained in both cases by air separation, and its energy demand is negligible compared to the whole process.

Ferenc KUBICSEK, Ferenc HEGEDŰS, Péter CSIZMADIA

The main aim of this study is to investigate an alternative way of ammonia production with microbubbles which initially contain nitrogen and hydrogen. If a liquid is irradiated with high-frequency and high-intensity ultrasound, micronsized bubbles are formed which are oscillating radially [6, 7]. This phenomenon is called as acoustic cavitation and serves as the basis of the scientific field known as sonochemistry [8–12]. During the radial pulsation, the collapse is very rapid. Therefore, the internal temperature can reach several thousands of kelvins inducing chemical reactions[13-22], which have been broadly investigated in the past decades both experimentally [23–25] and numerically [14, 26–31] where various combinations of liquid-gas compositions were considered with different levels of modelling complexities [32–36]. Unlike hydrodynamic cavitation, which is often considered detrimental due to material erosion and mechanical damage, and also causes redundant noise [22], acoustic cavitation can be beneficial by enabling localized extreme conditions for chemical reactions, which is the core principle of sonochemistry. In this situation, the internal pressure also increases, with the maximum value typically reaching thousands of bars. It is advantageous because it guarantees a high equilibrium concentration of ammonia during the collapse. The chemical yield depends on the initial gas content of the bubble, the reactions, the mass transfer via evaporation, condensation or diffusion.

In our previous study [29], the energy intensity of sonochemical ammonia synthesis was optimized under various conditions in water. Even in the best-case scenario, the energy intensity of the process was 719 GJ/t, which was still 18.4 times higher than the energy demand of the industrial Haber–Bosch process. This highlights a major limitation in the current sonochemical approach and motivates further research into enhancing energy intensity.

In sonochemistry, an interesting question is whether the use of non-Newtonian fluids can make this process more energy-efficient. Acoustically-excited non-Newtonian fluids were investigated widely [37–40], but, in these studies, chemical reactions were not explored. In our case, a single bubble is analyzed in a non-Newtonian fluid numerically, considering also the chemical reactions. The fluids are fictive materials that are similar to a mixture of water and Carbopol powder in several cases; see, e.g. [41]. Its fluid properties are summarized in Table 1. When selecting the fluid, several factors were considered. In our previous study [30], we observed that at a specific ambient pressure and density, increasing the sound speed

in the fluid positively influences the energy demand of ammonia production. In the present case, the fluid sound speed is higher than that of water, which makes it a suitable choice. Additionally, it was important that at an ambient pressure of 1000 bar, an apparent differential viscosity between 0.0002 and 0.1 Pa \cdot s has minimal impact on the energy demand. The consistency law index of the fluid in Table 1 is in this range. Similarly, variations in surface tension also have little effect on the overall energy requirements according to our previous study [30].

Parameter	Units	Value
$ ho_L$	kg/m ³	998.2
K	Pa · s ⁿ	0.07466
c_L	m/s	1600
σ	N/m	0.07197
n	_	0.7248

Table 1. Material properties of the applied non-Newtonian test fluid

In the governing equations, some approximations are used. The bubble interior is considered homogeneous, except for a thin thermal boundary layer which accounts for heat transfer across the bubble wall [42]. The bubble is assumed to have a perfectly spherical shape all the time [13, 43–49]. Because the oscillation period is very short, diffusion effects are neglected indeed [50].

The organization of this paper is as follows. In Section 2, the governing equations are introduced. In Section 3, the numerical technique and the control parameters are presented. In Section 4, the two most important concepts are defined which are necessary to understand the results: the chemical yield and the energy intensity. The results are introduced in Section 5. Section 6 concludes the paper.

2. Mathematical model

The mathematical model of a radially oscillating bubble can be separated into two main parts: a chemical and a physical model. In the physical model, the radial pulsation of the bubble and the temporal evolution of the temperature and pressure inside the bubble are described. In the chemical model, the chemical reactions are treated, where a large number of constants are needed to describe the reaction mechanism and the material properties. These constants are taken from [51] and are summarized in [52] as an OpenSMOKE++ reaction mechanism file according to [53, 54].

2.1. Introduction of the reaction mechanism

In this subsection, the chemical reaction mechanism and the types of the chemical reactions are introduced according to [29, 55, 56]. The importance of using

382

Ferenc KUBICSEK, Ferenc HEGEDŰS, Péter CSIZMADIA

appropriate reactions mechanisms for sonochemical applications is emphasized in [20].

The general form of a chemical reaction is the following:

$$\sum_{k=1}^{K} v_{ki}^{f} \chi_{k} = \sum_{k=1}^{K} v_{ki}^{b} \chi_{k}, \tag{1}$$

where v_{ki} denotes the stoichiometric coefficients and χ_k is the chemical symbol of the kth species. In the system, there are K types of species, which is why the summation runs from k = 1 to K. The index of the reactions is marked by i = 1, ..., I, where I is the number of the reactions. The forward and the backward reactions are marked by the upper index f and b, respectively. Note that a large amount of v_{ki}^f and v_{ki}^b are zero because not every species takes part in every reaction.

In reaction kinetics, the reaction rate indicates the speed of a reaction. For a given reaction, it can be positive, representing the dominance of the forward reaction, or negative, indicating that the reverse reaction is prevailing. The reaction rates can be calculated the following way:

$$q_i = k_{f_i} \sum_{k=1}^{K} c_k^{\gamma_{ki}^f} - k_{b_i} \sum_{k=1}^{K} c_k^{\gamma_{ki}^b},$$
 (2)

where k_{f_i} means the *i*th forward, and k_{b_i} means the *i*th backward reaction rate coefficients, and c_k denotes the concentration of the kth species. The next step is to calculate the production rates, which show the generation or consumption of a given species per unit time and per unit volume. The production rates $(\dot{\omega}_k)$ can be obtained by using the following equation:

$$\dot{\omega}_k = \sum_{i=1}^I \nu_{ki} q_i,\tag{3}$$

where $v_{ki} = v_{ki}^b - v_{ki}^f$. The *i*th forward rate coefficient is generally computed from the extended Arrhenius equation:

$$k_{f_i} = A_i T^{b_i} \exp\left(\frac{-E_i}{R_g T}\right). \tag{4}$$

In equation (4), A_i is the pre-exponential factor, T is the internal temperature, b_i is the temperature exponent, E_i is the activation energy, and $R_g = 8.31446 \,\mathrm{J/(mol \cdot K)}$ is the universal gas constant, respectively. Next, the equilibrium constants (K_{c_i}) have to be calculated:

$$K_{c_i} = K_{p_i} \left(\frac{P_{st}}{R_g T} \right)^{\sum_{i=1}^{I} \nu_{ki}}, \tag{5}$$



where the standard pressure (101325 Pa) is marked by $P_{\rm st}$. The K_{p_i} values are computed using the following equation:

$$K_{p_i} = \exp\left(\frac{\Delta S_i}{R_g} - \frac{\Delta H_i}{R_g T}\right),\tag{6}$$

where the change of entropy (ΔS_i) and enthalpy (ΔH_i) in the *i*th reaction can be obtained from

$$\frac{\Delta S_i}{R_g} = \sum_{k=1}^K \nu_{ki} \frac{S_i}{R_g} \tag{7}$$

and

$$\frac{\Delta H_i}{R_g T} = \sum_{k=1}^K \nu_{ki} \frac{H_i}{R_g T},\tag{8}$$

respectively. In equations (7) and (8), S_k and H_k denote the molar entropy and molar enthalpy of formation of the kth species at temperature T. The total change in a forward reaction (from reactants to products) is marked by Δ . The backward rate constants (k_{b_i}) can be obtained from

$$k_{b_i} = \frac{k_{f_i}}{K_{c_i}}. (9)$$

The Arrhenius equation describes most of the reactions preciously enough, but, in some cases, more accurate models are needed. The first type of such reactions is the three-body reactions, which are often dissociation or recombination reactions. These reactions require a third molecule to dissipate the excess energy of the energetically excited reaction intermediate. Any molecule in the system can act as a third body, but larger molecules are generally more effective. This efficiency can be accounted for using a third-body collision efficiency factor, which modifies the reaction rates as follows:

$$q_i' = q_i [M], (10)$$

where the effective total concentration of the third-body species is marked by [M] and can be calculated as

$$[M] = \sum_{k=1}^{K} \alpha_{ki} c_k. \tag{11}$$

In equation (11), α_{ki} is the matrix of the third-body efficiencies.

In some cases, the coefficient of the reaction rate depends on pressure (besides temperature). These reactions are called pressure-dependent reactions. The reaction rate coefficients in such cases are calculated here as follows: first, the high-pressure limit reaction rate coefficient (k_{∞}) and the low-pressure limit reaction rate coefficient (k_0) are computed using the following equations:

$$k_{\infty} = A_{\infty} T^{b_{\infty}} \exp\left(\frac{-E_{\infty}}{R_{o}T}\right)$$
 (12)

and

$$k_0 = A_0 T^{b_0} \exp\left(\frac{-E_0}{R_g T}\right). \tag{13}$$

From these values, the overall reaction rate constant is calculated the following way:

$$k'_{f_i} = k_{\infty} \frac{P_r}{1 + P_r} F,\tag{14}$$

where P_r is the reduced pressure written as

$$P_r = \frac{k_0}{k_\infty} \left[M \right],\tag{15}$$

and F is the blending function which determines the shape of the k'_{f_i} – P_r curve. In equation (14), the third-body efficiencies are already taken into account, therefore, the reaction rates have not to be multiplied by [M] once again. The next question is how to obtain F. There are several methods for it. In the Lindemann formalism, F = 1. Using the Troe formalism, F is obtained via the following equations:

$$\log_{10} F = \left[1 + \left[\frac{\log_{10} P_r + c}{n - d \left(\log_{10} P_r + c \right)} \right]^2 \right]^{-1} \log_{10} F_{\text{cent}}, \tag{16}$$

where F_{cent} denotes the broadening parameter

$$c = -0.4 - 0.67 \log_{10} F_{\text{cent}},\tag{17}$$

$$n = 0.75 - 1.27 \log_{10} F_{\text{cent}}, \tag{18}$$

$$d = 0.14,$$
 (19)

and

$$F_{\text{cent}} = (1 - \alpha) \exp\left(\frac{-T}{T^{***}}\right) + \alpha \exp\left(\frac{-T}{T^*}\right) + \exp\left(\frac{-T^{**}}{T}\right), \tag{20}$$

where α, T^{***}, T^* and T^{**} are the Troe parameters (they may vary for each Troeform reaction). In some cases, T^{**} is infinite; for this scenario, the last term in (20) is zero. Equations (16)-(20) implies that in the limiting cases, the forward reaction rate coefficient is the following:

$$k_{f_i} \to \begin{cases} k_{\infty}, & \text{if } p \to \infty, \\ k_0 [M], & \text{if } p \to 0, \end{cases}$$
 (21)

where p is the pressure. For some reactions, the pressure dependence of the reaction rate coefficient can be described by the PLOG-formalism. Here, an Arrhenius



 (A_j, β_j, E_j) set is given at several pressure levels (P_j) for each reaction. The forward reaction rate coefficient for the jth pressure level can be calculated as

$$k_j = k(T, P_j) = A_j T^{\beta_j} \exp\left(\frac{-E_j}{R_g T}\right). \tag{22}$$

For pressure values between P_j and P_{j+1} , the natural logarithm of k is obtained via a linear interpolation between the logarithm of the pressure levels (that is why this kind of reactions are called the PLOG reactions):

$$\ln k = \ln k_j + \frac{\ln p - \ln P_j}{\ln P_{j+1} - \ln P_j} \left(\ln k_{j+1} - \ln k_j \right). \tag{23}$$

Some reactions have the same reactants and products but follow two different temperature dependencies. These reactions can be represented using two separate Arrhenius equations and are termed duplicated reactions.

2.2. The physical model

The physical model consists of ordinary differential equations (ODEs). The radial oscillation of the spherical-assumed bubble is described by the modified Keller–Miksis equation [7]. In our case, the liquid is a power-law fluid, its flow curve is written as

$$\tau = K\dot{\gamma}^n. \tag{24}$$

Here, τ is the shear stress, K is the consistency index, $\dot{\gamma}$ is the shear rate, and n is the flow behavior index. Therefore, the Keller–Miksis equation has to be set up in the following form, assuming a power-law fluid:

$$\left(1 - \frac{\dot{R}}{c_L}\right) R \ddot{R} + \left(1 - \frac{\dot{R}}{3c_L}\right) \frac{3}{2} \dot{R}^2 =$$

$$= \left(1 + \frac{\dot{R}}{c_L} + \frac{R}{c_L} \frac{d}{dt}\right) \frac{1}{\rho_L} \left(p - \frac{2\sigma}{R} - \frac{4K\left(2\sqrt{3}\right)^{n-1}}{n} \left(\frac{\dot{R}}{R}\right)^n - p_{\infty}(t)\right), \quad (25)$$

according to [37] and [57]. In equation (25), the radius of the bubble is denoted by R, the time by t, the speed of sound in the liquid by c_L , and the density of the liquid by ρ_L , respectively. The connection between the internal pressure (p) and the liquid pressure at the bubble wall (p_L) is described by the following equation:

$$p = p_L + \frac{2\sigma}{R} + \frac{4K\left(2\sqrt{3}\right)^{n-1}}{n} \left(\frac{\dot{R}}{R}\right)^n. \tag{26}$$

386

The far-field pressure (p_{∞}) is constant, because the bubble oscillates freely:

$$p_{\infty}(t) = P_{\infty},\tag{27}$$

where the ambient pressure is marked by P_{∞} . The internal pressure is given by the ideal gas law for the gas mixture:

$$p = \sum_{k=1}^{K} c_k R_g T. \tag{28}$$

The time derivative of the temperature is computed using the first law of thermodynamics [29]:

$$\dot{T} = \frac{-p\frac{\dot{V}}{V} - \sum_{k=1}^{K} H_k \dot{\omega}_k + \sum_{k=1}^{K} \dot{\omega}_k R_g T + \frac{\dot{Q}_{th}}{V}}{\sum_{k=1}^{K} c_k \overline{C}_v},$$
(29)

where $V = 4R^3\pi/3$ is the volume of the bubble, \dot{Q}_{th} is the heat transfer at the bubble interface, and C_v is the average molar heat capacity of the gas mixture in the bubble at constant volume. The molar heat capacity at constant pressure $C_{p,k}$, the molar enthalpy of formation H_k and the molar entropy S_k of the chemical species can be calculated from the NASA polynomials using the following equations [56]:

$$\frac{C_{p,k}}{R_g} = \sum_{n=1}^{N} a_{n,k} T^{n-1},\tag{30}$$

$$\frac{H_k}{R_g T} = \sum_{n=1}^{N} \frac{a_{n,k} T^{n-1}}{n} + \frac{a_{N+1,k}}{T},\tag{31}$$

and

$$\frac{S_k}{R_g} = a_{1,k} \ln (T) + \sum_{n=1}^{N} \frac{a_{n,k} T^{n-1}}{n-1} + a_{N+1,k},$$
(32)

where N=5, and the NASA coefficients are marked by $a_{n,k}$. For every species, two sets of coefficients are given: one set for the interval $[T_{\text{low}}, T_{\text{mid}}]$ and one for the interval $[T_{\text{mid}}, T_{\text{high}}]$. The isochor molar heat capacities $(C_{v,k})$ can be calculated from the following equation:

$$C_{v,k} = C_{p,k} - R_g. \tag{33}$$

For the further calculations, some average values of the gas mixture is needed. The mole fraction of the *k*th component is given by

$$X_k = \frac{c_k}{\sum\limits_{k=1}^K c_k}. (34)$$



The average molar mass (\overline{M}) , the average molar heat capacity at constant pressure (\overline{C}_p) and at constant volume (\overline{C}_v) , and the average density $(\overline{\rho})$ are computed by:

$$\overline{M} = \sum_{k=1}^{K} X_k M_k, \tag{35}$$

$$\overline{C}_p = \sum_{k=1}^K X_k C_{p,k},\tag{36}$$

$$\overline{C}_{v} = \sum_{k=1}^{K} X_k C_{p,v},\tag{37}$$

and

$$\overline{\rho} = \sum_{k=1}^{K} c_k M_k. \tag{38}$$

In equations (35)-(38), the molar mass of the kth species is denoted by M_k . The bars represent the averaged values for the mixture.

The heat transfer through the bubble wall is described by the Toegel model [42]. This model assumes that outside of the bubble the temperature is equal to the ambient temperature ($T_0 = 293.15 \, \text{K}$). Inside the bubble, the temperature is the internal temperature (T) except for a thin thermal boundary layer. In this layer, the temperature changes linearly. Using this model, the heat transfer can be approximated as

$$\dot{Q}_{th} = A\overline{\lambda}\frac{\partial T}{\partial r} = A\overline{\lambda}\frac{T_0 - T}{l_{th}},\tag{39}$$

where A denotes the area of the bubble surface, $\overline{\lambda}$ is the average thermal conductivity of the gas mixture, and l_{th} is the thickness of the boundary layer, which can be approximated as

$$l_{th} = \min\left(\sqrt{\frac{R\overline{\chi}}{\dot{R}}}, \frac{R}{\pi}\right),\tag{40}$$

where the averaged thermal diffusivity of the mixture $(\overline{\chi})$ is obtained by

$$\overline{\chi} = \frac{\overline{\lambda}}{\overline{\rho}\overline{C}_p}\overline{M}.\tag{41}$$

The heat produced and consumed in the reactions (reaction enthalpies) are already taken into consideration, therefore, the heat transfer consist of only the heat conduction:

$$\sum \dot{Q} = \dot{Q}_{th}.\tag{42}$$

2.3. Structure of the equation system

The governing equations compose an ordinary differential equation system with the following structure. The radial oscillation of the bubble is modelled by the Keller–Miksis equation: its solution is the temporal evolution of the bubble radius R. The temporal evolution of the temperature is computed by the first law of thermodynamics, where the reaction enthalpies, the work done by the compression and the heat transfer through the bubble wall are taken into consideration. Using the reaction mechanism introduced in Section 2.1, K ODEs are obtained for the concentrations of the chemical species inside the bubble:

$$\dot{c}_k = \dot{\omega}_k - c_k \frac{\dot{V}}{V}.\tag{43}$$

During the simulations, it is supposed that the liquid is non-volatile, and initially, the bubble contains only nitrogen and hydrogen. Therefore, only reactions involving elements N and H occur. That is why the system incorporates I=36 chemical reactions and K=14 chemical species. The mechanism file contains all the reactions for the complete N-H-O system but the reactions involving O are commented out because of this assumption.

Altogether, the system consists of K + 3 differential equations: two first-order ordinary differential equations from the Keller–Miksis equation (which is a second-order ODE), a first-order ODE for the internal temperature, and K first-order ODEs for the change of concentrations.

To close the equation system, an algebraic equation is needed, which is the ideal gas law. This makes connection between the volume, the internal temperature and the internal pressure. Because the volume is computed from the bubble radius *R* and the temperature from the first law of thermodynamics, the ideal gas law is used in order to obtain the internal pressure.

3. Control parameters and numerical method

The main control parameters of a freely oscillating spherical bubble system are the equilibrium size of the bubble R_E ; the expansion ratio R_0/R_E , where R_0 denotes the initial size of the bubble at the beginning of the simulations, which is also the maximum bubble radius; the initial mole fraction of hydrogen in terms of percentage; and finally, the ambient pressure P_{∞} . The effect of varying the sound speed of the liquid c_L , the flow behavior index n and the consistency index n are also explored. The applied ranges of these control parameters are summarized in Table 2.

The reason for selecting these control parameters is the following. The equilibrium bubble size influences the initial amount of nitrogen and hydrogen gas inside the bubble: bubbles with larger equilibrium size contain more substances which can react with each other. However, the bubble radius should not be greater



Table 2. Summary of the control parameters and their employed ranges during the simulations

$R_E (\mu m)$	R_0/R_E	P_{∞} (bar)	Н%	c_L (m/s)	n	$K(Pa \cdot s)$
1-10000	3-11	1-1000	65-85	1483;	0.25; 0.5; 0.7248	0.0001; 0.001; 0.01;
1-10000	3-11 1-1000	1-1000		1600	1.25; 1.5	0.07466; 0.1; 1; 10; 100

than 10 mm, otherwise the spherical stability of the bubble would be very poor [7, 13]. The expansion ratio is in connection with the initial potential energy of the bubble; it is introduced in more detail in Section 4. This energy is responsible for the extreme temperature and pressure at the first collapse of the bubble. In the long term, it is dissipated by the viscous forces during the oscillation. The reason for varying the mole fraction is the following: from stoichiometric considerations, the optimal initial mixture in the bubble would be 75% hydrogen and 25% nitrogen. Nevertheless, the initial composition of the bubble may not be fully converted into ammonia, because the time scale of the extreme conditions is short and the reaction pathway is very complex; it involves also intermediates such as NH and NH₂. Therefore, the energy intensity may be better if the initial gas composition differs from the stoichiometric mixture. The importance of the ambient pressure is reflected in the amount of the input energy. The biggest part of it is the energy needed to displace the volume of the surrounding liquid: less displacement needs significantly less input energy, see in Section 4. However, ambient pressure also influences the bubble dynamics: increasing the ambient pressure makes the temperature and pressure peak wider, facilitating the ammonia conversion. It is an interesting question, which effect is more dominant in a specific case. The ambient pressure needs to be limited at 1000 bar because typical engineering applications operate up to this value. The effect of sound speed is also analyzed because an important result was in [30] that it can substantially affect on the energy intensity. Finally, the flow behavior index and the consistency index affect the viscous dissipation in a nontrivial way. At lower values of these parameters, the apparent viscosity is small during high-velocity phases of the oscillation, which leads to faster bubble motion. However, this also implies that the bubble cannot collapse to very small radii, as a significant portion of the energy is dissipated before strong compression occurs. As a result, the peak temperature remains low and the chemical yield is poor. In contrast, higher values of the rheological parameters increase the viscous resistance, slowing down the motion but allowing the bubble to spend more time in a compressed state. This favors higher peak temperatures and longer reaction durations, which may improve the ammonia conversion. The balance between dissipation and confinement time remains a key question to be addressed.

The differential equation system is stiff, that is why it is solved in Python using LSODA and Radau method, which are stiff solvers. The full program code can be accessed at [58]. We ensure that the optimal values do not fall on the upper or lower boundaries of the specified parameters.



4. Definition of the chemical yield and the energy intensity

Ferenc KUBICSEK, Ferenc HEGEDŰS, Péter CSIZMADIA

In Fig. 1, typical time curves of a freely oscillating bubble are depicted. The top panel shows the bubble radius (blue) and the internal temperature (red) versus time. The equilibrium radius of the bubble is 50 µm, and the initial expansion is 7. At the beginning of the simulation, the bubble starts to collapse because its size is bigger than the equilibrium radius. Because of the inertia of the surrounding liquid, the bubble radius swings through its equilibrium value resulting in a large compression ratio. The peak temperature at the minimal radius is almost 6000 K. After the first collapse, the bubble emits a shock wave from itself, consequently, it loses most of its energy. This phenomenon is called the acoustic emission [59]. Therefore, the second local maximum temperature is much lower than the first one, the amplitude of the oscillations gradually decreases afterward, and the dynamics of the bubble converges to its equilibrium state. In the bottom panel of Fig. 1, the temporal evolution of the chemical species inside the bubble is depicted in moles (n_k) . The initial content of the bubble consists of only nitrogen and hydrogen, but, during the first collapse, around the minimum bubble radius, a small part of the hydrogen dissociates and other chemical species are formed. Nevertheless, most of the nitrogen (dashed red curve) and the hydrogen (solid orange curve) remain intact. The main product of the reactions is ammonia (bold blue curve). The other chemical species appear with orders of magnitude lower concentration, which is advantageous for the energy intensity of producing ammonia. The chemical yield

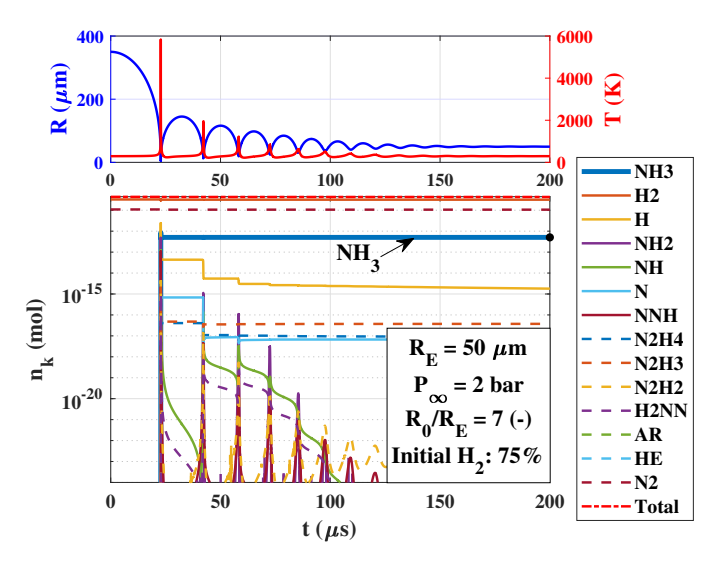


Fig. 1. Time curves of a freely oscillating bubble. Top panel: the temporal evolution of the bubble radius and the internal temperature, bottom panel: the amount of chemical species in the bubble as a function of time (the red dash-dotted line represents the total amount of species in the bubble in moles). The equilibrium bubble radius is $50 \, \mu m$, the ambient pressure is 2 bar, the initial expansion ratio is 7 and the initial mole fraction of hydrogen and hydrogen are 75% and 25%, respectively



of a bubble is defined as the amount of ammonia $(n_{\rm NH_3})$ present inside the bubble once chemical equilibrium is reached. This corresponds to the final time instant of the simulation, represented by the black dot on the bold blue curve in the bottom panel of Fig. 1.

The mass of the produced ammonia is obtained via

$$m_{\rm NH_3} = n_{\rm NH_3} M_{\rm NH_3},\tag{44}$$

where $M_{\rm NH_3}$ denotes the molar mass of ammonia.

The energy needed to expand the bubble from the equilibrium radius R_E to the maximum radius R_0 (or, in other words, the potential energy, W_P) consists of three parts [29]:

$$W_P = W_G + W_A + W_L, \tag{45}$$

The first term in (45) is the physical work done on the internal gas, assuming that the expansion is slow (therefore, the process is isothermic):

$$W_G = -N_{t,0} R_g T_E \ln \left(\frac{R_0^3}{R_E^3} \right), \tag{46}$$

where the initial amount of gas in moles is marked by $N_{t,0}$. The second term is the work which is required to enlarge the surface of the bubble against the surface tension:

$$W_A = \sigma 4\pi \left(R_0^2 - R_E^2 \right). \tag{47}$$

And, the last term is the work needed to expand the bubble against the liquid domain:

$$W_L = P_\infty \frac{4\pi}{3} \left(R_0^3 - R_E^3 \right). \tag{48}$$

This work is required to displace the volume of the liquid against the ambient pressure.

The hydrogen as a primary commodity also needs energy to be produced, which has to be taken into account. It is assumed that the hydrogen is produced via electrolysis. According to [29], its energy requirement is

$$w_{\rm H_2} = m_{\rm H/NH_3} W_E = \frac{3M_{\rm H}}{M_{\rm NH_3}} W_E,$$
 (49)

where $m_{\rm H/NH_3}$ denotes the mass fraction of atomic hydrogen in ammonia molecule (its unit is tH/t NH₃), $M_{\rm H}$ is the molar mass of hydrogen, and $W_E = 180\,{\rm GJ/t}$ is the energy needed for the electrolysis of water.

If the ambient pressure is higher than the atmospheric pressure, the initial bubble content needs to be pressed into the reaction chamber. As stated in [29], its energy requirement is given as

$$w_p = R_{N_2 H_2} T \ln \left(\frac{P_{\infty}}{P_{st}} \right), \tag{50}$$

where the index p suggests that it is a pressing energy, and

$$R_{\rm N_2H_2} = \frac{R_{\rm N_2} M_{\rm N_2} X_{\rm N_2} + R_{\rm H_2} M_{\rm H_2} X_{\rm H_2}}{M_{\rm N_2} X_{\rm N_2} + M_{\rm H_2} X_{\rm H_2}},$$
(51)

where the specific gas constants are $R_{\rm N_2} = 297 \, {\rm J/(kg \cdot K)}$ and $R_{\rm H_2} = 4124 \, {\rm J/(kg \cdot K)}$ [29].

The total input energy of the bubble system consists of three main components: the energy required to expand the bubble, the energy needed to produce the hydrogen content, and the energy for pressing. This total energy requirement (w_{TR} , expressed in GJ/t) can be obtained by

$$w_{TB} = \frac{W_P}{m_{\text{NH}_3}} + w_{\text{H}_2} + w_p. \tag{52}$$

Equation (52) strongly depends on the system parameters. For comparison, the energy intensity of the Haber-Bosch process, when hydrogen is produced via electrolysis, is $w_{\rm HB} = 39.1 \, {\rm GJ/t}$ [60]. During parameter optimization, this value serves as the reference for assessing the energy intensity of ammonia production using bubbles.

5. Results of the parameter studies

This section examines the energy intensity as a function of the control parameters defined in Section 3, using the quantities introduced in Section 4. In Fig. 2, the energy intensity is depicted as a function of the equilibrium bubble radius at several initial expansion ratios (color-coded curves). Here, the ambient pressure is 1 bar and the initial gas mixture is stoichiometric (75% H₂ and 25% N₂). The horizontal red and blue lines represent the energy intensity of the Haber–Bosch process. The optimal parameters and energy intensity are the following: $R_E = 45.35 \,\mu\text{m}$, $R_0/R_E = 6$ and $w_{TB} = 1936.2$ GJ/t, which is 49.5 times higher than that of the Haber-Bosch process. However, this value is 10.8% better than the optimal energy intensity at 1 bar in water [29] (2145 GJ/t).

In an idealistic case, the optimal initial gas composition of the bubble is 75% H₂ and 25% N₂, considering that all molecules participate in the formation of ammonia. Nevertheless, in our case, as it can be already seen in Fig. 1, a large amount of the reagents do not take part in the reactions. For example, the initial amount of hydrogen in the bubble is $3.269 \cdot 10^{-11}$ mol, which decreases to $3.193 \cdot 10^{-11}$ mol by the end of the simulation. This corresponds to a consumption of approximately 2.3% of the initial hydrogen content. Since ammonia formation involves the dissociation of H₂ and subsequent reactions of intermediates like NH and NH₂, optimizing the initial mole fractions of nitrogen and hydrogen could potentially enhance these intermediate reactions and improve energy efficiency. Fig. 3 shows the energy intensities for 65, 75 and 85% initial hydrogen content

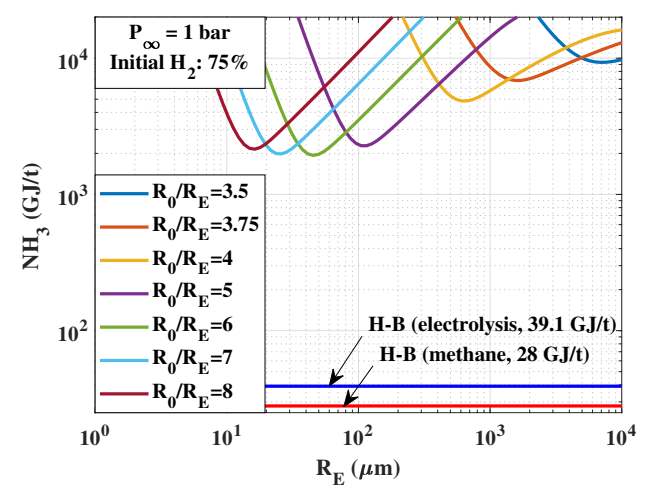


Fig. 2. Energy intensity of ammonia production as a function of the equilibrium bubble radius at different initial expansion ratios. The ambient pressure is 1 bar, and the initial gas mixture is stoichiometric (75% H₂ and 25% N₂). The blue and red lines represent the energy intensity of the Haber–Bosch process if the hydrogen comes from the electrolysis of water and from methane, respectively

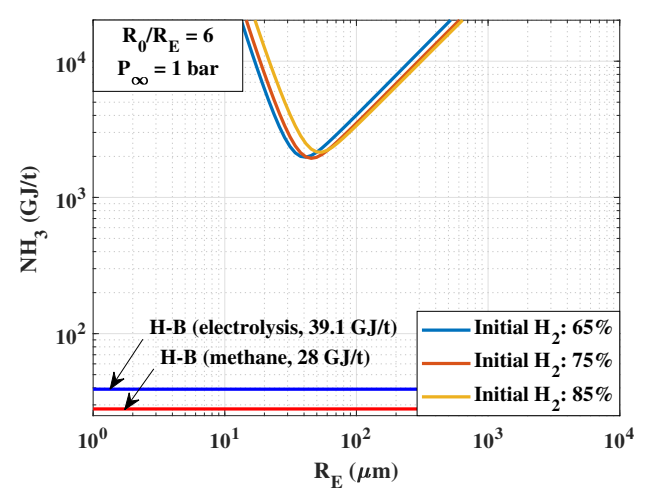


Fig. 3. Energy intensity of ammonia production as a function of the equilibrium bubble radius at different initial hydrogen mole fractions. The ambient pressure is 1 bar, and the initial expansion ratio is 6. The blue and red lines represent the energy intensity of the Haber–Bosch process if the hydrogen comes from the electrolysis of water and from methane, respectively

at the best initial expansion ratio from Fig. 2 and at the same ambient pressure (1 bar). From Fig. 3, one can see that the best mole fraction of hydrogen is still 75%, similarly to [29], as the lowest energy intensity in the figure corresponds to this hydrogen mole fraction.



In the next step, the value of the ambient pressure is optimized. In these simulations, the initial mole fractions of hydrogen and nitrogen are 75% and 25%, respectively (according to the best case in Fig. 3). Plots similar to Fig. 2 are generated for various ambient pressures, each showing seven initial expansion ratios to maintain clarity and avoid overcrowding. The results are depicted in Fig. 4. Similarly to [29], the bubble dynamics can change significantly if the ambient pressure is increased; therefore, the time curve of the internal temperature and the intensity of the chemical reactions are also affected. As mentioned before, the upper limit of the bubble size is 10 mm otherwise the bubble will have poor spherical stability [7, 13].

From Fig. 4, it can be seen that the optimal energy intensity improves if the ambient pressure is increased (similarly to [29]), but here, the best energy intensity is somewhat better, $682.6\,\mathrm{GJ/t}$, which is 17.46-fold that of the Haber–Bosch process (it is 5.3% better than the optimal value of $719\,\mathrm{GJ/t}$ in [29], but it is much worse than the optimal value of $234.42\,\mathrm{GJ/t}$ in [30]). The optimal parameters in the investigated range are $R_E = 2983.7\,\mu\mathrm{m}$, $R_0/R_E = 6$ and $P_\infty = 1000\,\mathrm{bar}$. The optimal parameter combinations and energy intensities are summarized in Table 3. In some cases, the simulation cannot run, especially at high ambient pressures; that is why the initial sections of these curves (where the equilibrium bubble radius is small) are missing.

The maximal ambient pressure applied here is 1000 bar, which is much higher than the operating pressure of the Haber–Bosch process. However, in this study, only the theoretical energy intensity limits are investigated, therefore, higher ambient pressures than that of the Haber-Bosch process are allowed. Most of the optimal bubble sizes are also bigger than 1 mm: these bubble are large and can collapse in non-spherical state. Nevertheless, the long-term spherical stability of the bubble is not necessary, the bubble needs to withstand only a single collapse. In our model, it is assumed that the primary chemical reactions occur during the first collapse, in which the bubble is expected to remain approximately spherical. Therefore, as long as the bubble retains structural integrity up to this point, possible nonspherical effects during subsequent oscillations are not expected to significantly influence the simulated energy intensity. Therefore, these cases are also included in Table 3. The optimal expansion ratios vary in the range of 4-6 (similarly to [29]). The tendency of the energy intensity as a function of the ambient pressure is summarized in Fig. 5. Similarly to [29], approximately above 10 bar ambient pressure, the energy intensity declines rapidly but the value tends to approximately 680 GJ/t which is somewhat lower than the saturation level of 700 GJ/t in [29].

The question arises, what the reason is for the improvement of the optimal energy intensity in comparison to [29]: the non-Newtonian behavior or the higher sound speed (in [29], water was applied, where the sound speed was $c_L = 1483 \,\mathrm{m/s}$). To investigate it, the plots in Fig. 4 at 1000 bar are made also at the sound speed in water. The other parameters of the liquid presented in Table 1

ww.journals.pan.pl

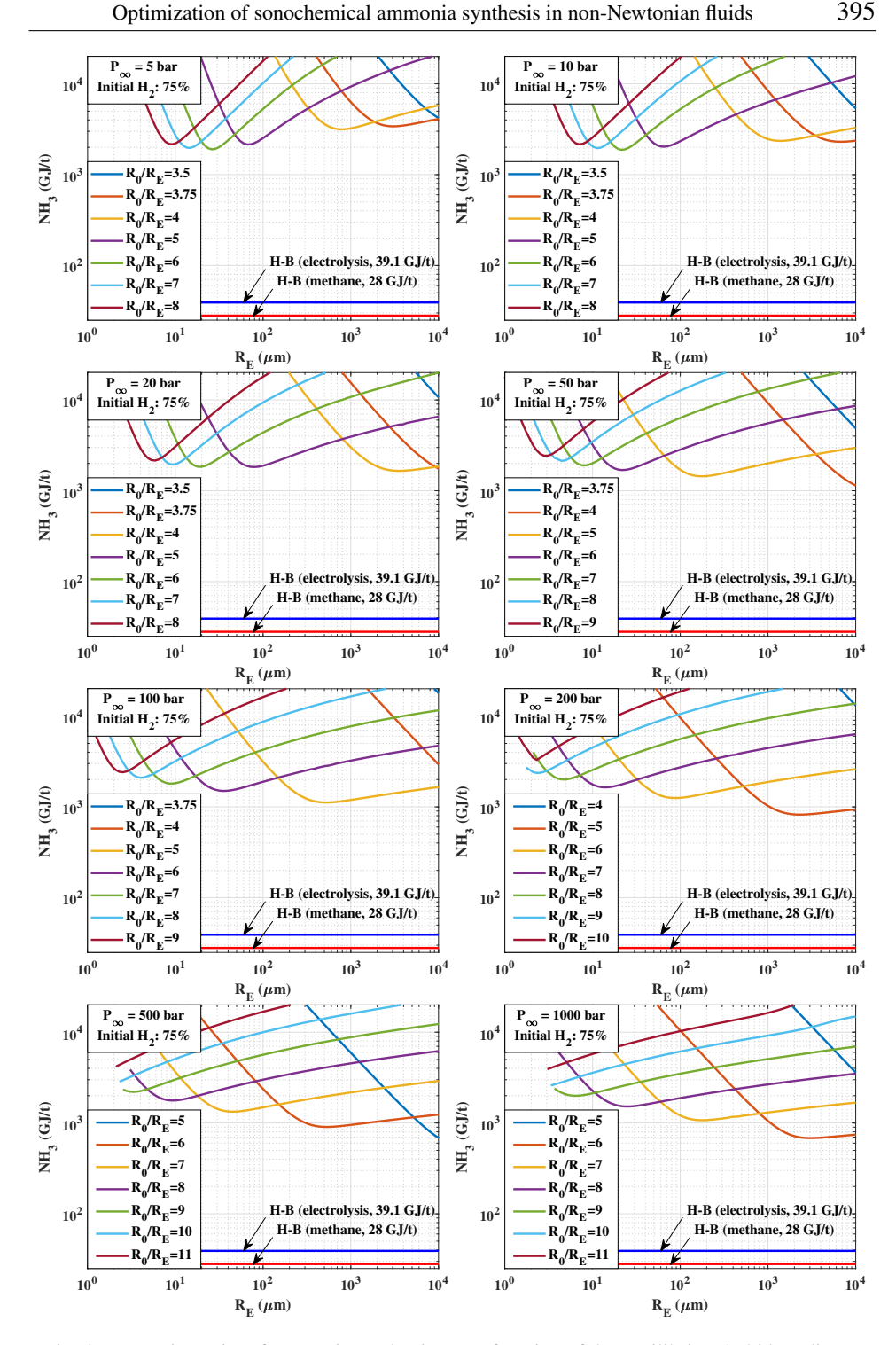


Fig. 4. Energy intensity of ammonia production as a function of the equilibrium bubble radius at different initial expansion ratios and ambient pressures. The initial mixture is always 75% H $_2$ and 25% N $_2$. The blue and red lines represent the energy intensity of the Haber–Bosch process if the hydrogen comes from the electrolysis of water and from methane, respectively

		1	_
P_{∞} (bar)	R_E^{opt} (µm)	$(R_0/R_E)^{\text{opt}}$ (-)	w_{TB}^{opt} (GJ/t)
5	25.95	6	1900.0
10	21.54	6	1875.5
20	3593.8	4	1655.9
50	10000	4	1141.5
100	509.4	5	1118.9
200	2257.0	5	822.5
500	10000	5	686.4
1000	2983.7	6	682.6

Table 3. Summary of the optimal parameters and the optimal energy intensity at the ambient pressure used in Fig. 4

are not altered. The energy intensities as a function of the equilibrium radius are depicted in Fig. 6. Results show that in this case, the optimal energy intensity is 719 GJ/t, which is the same as the corresponding value in [29]. Therefore, the energy improvement in Fig. 4 is caused by the increment of the sound speed.

Next, the effect of varying the flow behavior index is analyzed at the best ambient pressure (1000 bar), as the non-Newtonian nature of the fluid could theoretically influence the energy intensity. Therefore, the same simulations are made as in Fig. 4 at 1000 bar, but the flow behavior indices are 0.25, 0.5, 1.25 and 1.5. The results are shown in Fig. 7, the optimal parameters and energy intensities are summarized in Table 4. From the figures and the table one can see that the energy intensities at the n > 1 values are somewhat worse than at the original value, n = 0.7248; and, the system also responds more sensitively to the changes of the equilibrium bubble radius. The optimal energy intensity marginally improves if n is smaller than the

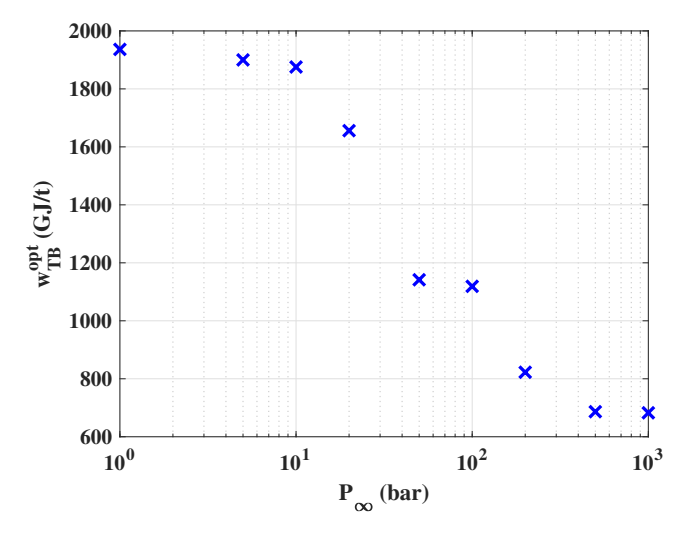


Fig. 5. The optimal energy intensity of the ammonia production as a function of the ambient pressure

397

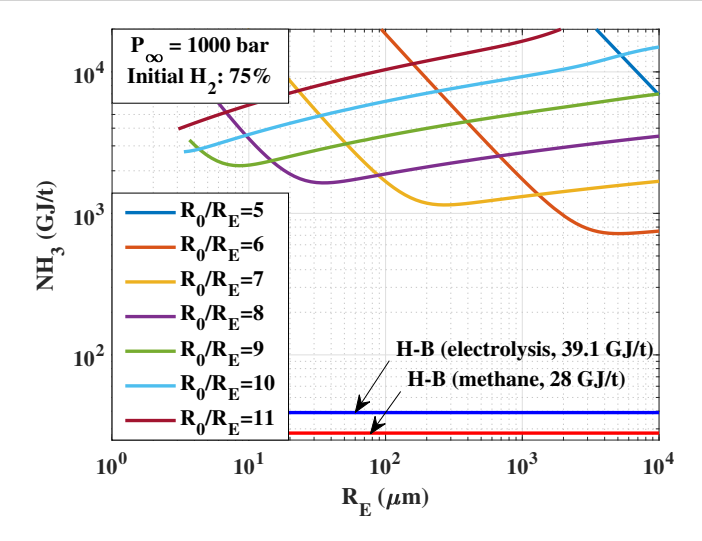


Fig. 6. Energy intensity of ammonia production as a function of the equilibrium bubble radius at different initial expansion ratios. The ambient pressure is 1000 bar, and the initial gas mixture is stoichiometric (75% $\rm H_2$ and 25% $\rm N_2$). The sound speed equals to the value in water ($c_L=1483~\rm m/s$), the other parameters of the liquid are taken from Table 1. The blue and red lines represent the energy intensity of the Haber–Bosch process if the hydrogen comes from the electrolysis of water and from methane, respectively

initial value, but it is not significant. The best energy intensity is at n = 0.25, its value is $682.601 \,\text{GJ/t}$ which is 17.5-fold that of the Haber–Bosch process. This is the best energy intensity observed in the study.

Finally, the impact of varying the consistency index is investigated. Here, the simulations in Fig. 4 are rerun with K = 0.0001, 0.001, 0.01, 0.1, 1, 10, and 100 at 1000 bar ambient pressure. To maintain clarity, only the optimal parameters and the best energy intensities are presented, as listed in Table 5. The results indicate that increasing the consistency index leads to only a slight deterioration in energy performance. This trend aligns with our previous findings in [30], where viscosity showed negligible influence on energy intensity at this pressure level.

Table 4. Summary of the optimal parameters and the optimal energy intensity as a function of the flow behavior index. The ambient pressure is 1000 bar, the other parameters of the liquid are taken from Table 1

n (-)	R_E^{opt} (μ m)	$(R_0/R_E)^{\text{opt}}$ (-)	$w_{TB}^{\text{opt}} \text{ (GJ/t)}$
0.25	2983.7	6	682.601
0.5	2983.7	6	682.602
0.7248 (original)	2983.7	6	682.604
1.25	2983.7	6	684.029
1.5	4328.8	6	701.776

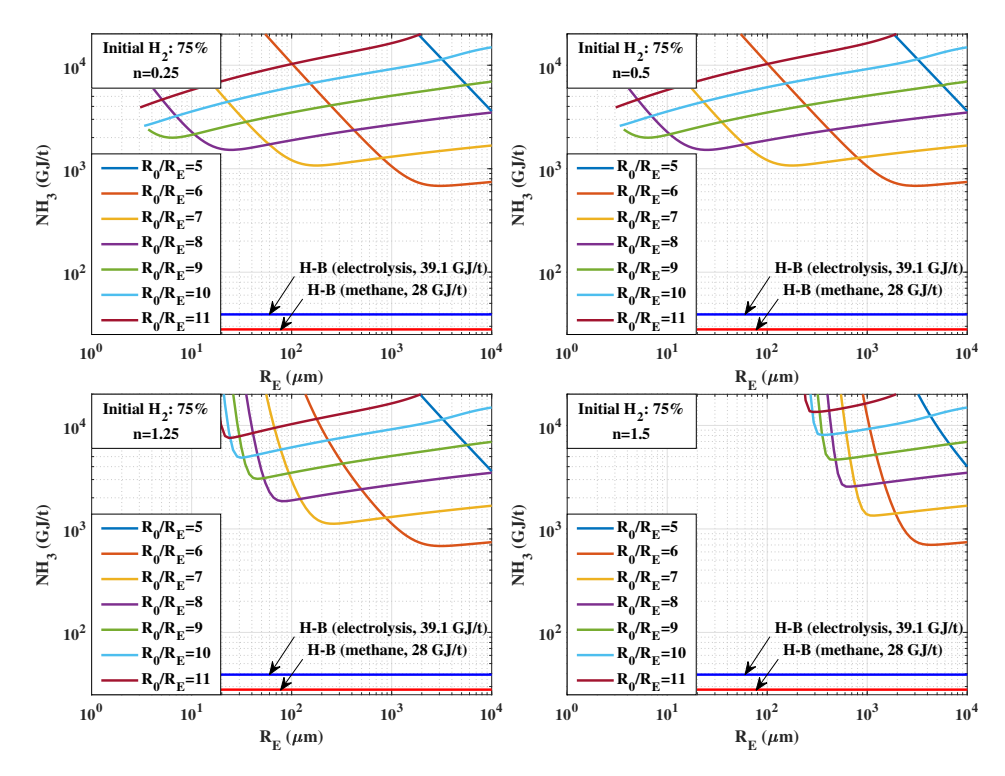


Fig. 7. Energy intensity of ammonia production as a function of the equilibrium bubble radius at different initial expansion ratios and flow behavior indices. The other parameters of the liquid are taken from Table 1. The initial mixture is always 75% H₂ and 25% N₂, the ambient pressure is 1000 bar. The blue and red lines represent the energy intensity of the Haber-Bosch process if the hydrogen comes from the electrolysis of water and from methane, respectively

Table 5. Summary of the optimal parameters and the optimal energy intensity as a function of the consistency index. The ambient pressure is 1000 bar, the other parameters of the liquid are taken from Table 1

R_E^{opt} (µm)	$(R_0/R_E)^{\text{opt}}$ (-)	w_{TB}^{opt} (GJ/t)
2983.7	6	682.601
2983.7	6	682.602
2983.7	6	682.602
2983.7	6	682.604
2983.7	6	682.605
2983.7	6	682.632
2983.7	6	682.913
3274.6	6	685.348
	2983.7 2983.7 2983.7 2983.7 2983.7 2983.7 2983.7	2983.7 6 2983.7 6 2983.7 6 2983.7 6 2983.7 6 2983.7 6 2983.7 6 2983.7 6



6. Conclusions

The main goal of the present paper was to investigate the theoretical energy intensity of ammonia production via a freely oscillating microbubble, which is placed in non-Newtonian test fluids and initially contains nitrogen and hydrogen. The chemical yield of ammonia is calculated using numerical simulations, where the chemical reactions are analyzed in the bubble. The input energy is obtained as the sum of the potential energy of the initially expanded bubble, the energy needed to produce hydrogen via electrolysis of water and the energy required to press the initial mixture into the reaction chamber. The control parameters were the equilibrium bubble radius, the initial expansion ratio, the initial mole fraction of hydrogen, the ambient pressure, the sound speed in the liquid and the flow behavior index. At the optimal parameter combination, the energy intensity of ammonia production was 682.601 GJ/t. Compared to [29] (where the optimal energy intensity was 719 GJ/t), it is a 5.3% improvement. This energy intensity of 682.601 GJ/t is 17.5-fold higher than that of the Haber–Bosch process (its energy intensity is in the best case 39.1 GJ/t if the hydrogen source is water electrolysis), but, similarly to [29], this value is several orders of magnitude better than [23] (882353 GJ/t). The reason is explained in [29]: while continuously exciting the system in [23], after the first three or four acoustic cycles, only the energy of the reactor is dissipated without useful chemical reactions.

The question was what the reason was for this 5.3% improvement compared to [29]. The observed improvement is primarily attributed to the increase in the liquid sound speed c_L rather than the modification of the flow behavior index n or the consistency index K. The analysis indicates that the enhancement in energy intensity is mainly driven by the higher speed of sound c_L , while decreasing in the flow behavior index n and the consistency index K has no significant impact on the results. Nevertheless, increasing the flow behavior index above 1 or the consistency index above $0.1 \, \text{Pa} \cdot \text{s}$ would be moderately detrimental, leading to higher energy intensity and weaker process performance.

Summarizing the results, ammonia production using microbubbles can still be feasible; nevertheless, for lower energy intensity than the Haber–Bosch process and for exploiting the potential environmental advantages of the sonochemical process, the operation strategy needs to be reevaluated before scaling up the process to the industrial level. For this purpose, the optimization of the excitation waveform of an ultrasound irradiation can be a good starting point. The simplest example is a simple sinusoidal wave, where the initial rarefaction phase expands the bubble and the subsequent compression phase triggers collapse. After the impulse ends, the bubble undergoes free oscillation. This scenario closely resembles the present model, but its detailed analysis lies beyond the current scope. Alternatively, energy intensity might be improved by utilizing bubble–bubble interactions, which could enhance the local pressure and temperature fields through constructive interference effects. However, their impact is highly system-dependent and not explicitly accounted for

in the present model [61]. Further work using multi-bubble simulations would be needed to assess their role under realistic excitation conditions. Another promising route is to target the direct synthesis of fertilizing compounds, such as ammonium nitrate (NH₄NO₃), thereby eliminating the need for downstream processing and improving the overall process viability. There are also challenges in bubble control and acoustic field propagation in non-Newtonian fluids complicate scalability, which have to be addressed as well. However, since the tested non-Newtonian fluids did not lead to improved energy efficiency, addressing these challenges in such media is not a priority at this stage.

Acknowledgements

The research was supported by the EKÖP-24-3-BME-234 University Research Fellowship Programme of the Ministry for Culture and Innovation from the source of the National Research, Development and Innovation Fund. The authors acknowledge the financial support of the Hungarian National Research, Development and Innovation Office via NKFIH grant OTKA FK-142376.

References

- [1] International Energy Agency (IEA). Ammonia technology roadmap: Executive summary, 2024. Accessed: 2025-03-03. URL: https://www.iea.org/reports/ammonia-technology-roadmap/executive-summary.
- [2] D. Cheddie. Ammonia as a hydrogen source for fuel cells: ArReview. In *Hydrogen Energy—Challenges and Perspectives*, chapter 13, pages 333–362. Intech, 2012. doi: 10.5772/47759.
- [3] A. Valera-Medina, H. Xiao, M. Owen-Jones, W.I.F. David, and P.J. Bowen. Ammonia for power. *Progress in Energy and Combustion Science*, 69:63–102, 2018. doi: 10.1016/j.pecs.2018.07.001.
- [4] International Renewable Energy Agency. Innovation outlook: Renewable ammonia, 2022. URL: https://www.irena.org/publications/2022/May/Innovation-Outlook-Renewable-Ammonia.
- [5] F. Ausfelder, E.O. Herrmann, and L.F. López González. Perspective Europe 2030: Technology options for CO₂-emission reduction of hydrogen feedstock in ammonia production, 2022. URL: https://dechema_de/dechema_media/Downloads/Positionspapiere/Studie+Ammoniak.pdf.
- [6] T. G. Leighton. The Acoustic Bubble. Academic Press, 2012. doi: 10.1016/B978-0-12-441920-9.X5001-9.
- [7] W. Lauterborn and T. Kurz. Physics of bubble oscillations. Reports on Progress in Physics, 73(10):106501, 2010. doi: 10.1088/0034-4885/73/10/106501.
- [8] L. Lv, F. Liu, and Y. Li. Numerical study on the dynamics of a charged bubble in the acoustic field. *Archives of Acoustics*, 49(2):233–240, 2024. doi: 10.24425/aoa.2024.148786.
- [9] A. Salaeh. Influence of ultrasonic cavitation on *Botryococcus braunii* growth. *Archives of Acoustics*, 49(3):439–445, 2024. doi: 10.24425/aoa.2024.148800.
- [10] M. Huang, S. Jin, G. Nie, X. Wang, Q. Zhang, Y. An, Z. Qu, and W. Yin. Removal of fouling from steel plate surfaces based on multi-frequency eco-friendly ultrasonic guided wave technology. *Archives of Acoustics*, vol. 48(No 4):593–601, 2023. doi: 10.24425/aoa.2023.146644.



- [11] W.C. Hong, Y.Y. Kim, C.D. Kwon, and K.C. So. Effects of ultrasonic power and intensity of mechanical agitation on pretreatment of a gold-bearing arsenopyrite. *Archives of Acoustics*, 49(3):419–428, 2024. doi: 10.24425/aoa.2024.148801.
- [12] M. Piątek and A.M. Bartkowiak. Effectiveness of using physical pretreatment of lignocellulosic biomass. *Journal of Water and Land Development*, (58):62–69, 2023. doi: 10.24425/jwld.2023.146598.
- [13] C. Kalmár, K. Klapcsik, and F. Hegedűs. Relationship between the radial dynamics and the chemical production of a harmonically driven spherical bubble. *Ultrasonics Sonochemistry*, 64:104989, 2020. doi: 10.1016/j.ultsonch.2020.104989.
- [14] K. Yasui, T. Tuziuti, T. Kozuka, A. Towata, and Y. Iida. Relationship between the bubble temperature and main oxidant created inside an air bubble under ultrasound. *The Journal of Chemical Physics*, 127(15), 2007. doi: 10.1063/1.2790420.
- [15] L. Stricker and D. Lohse. Radical production inside an acoustically driven microbubble. Ultrasonics Sonochemistry, 21(1):336–345, 2014. doi: 10.1016/j.ultsonch.2013.07.004.
- [16] K. Kerboua and O. Hamdaoui. Influence of reactions heats on variation of radius, temperature, pressure and chemical species amounts within a single acoustic cavitation bubble. *Ultrasonics Sonochemistry*, 41:449–457, 2018. doi: 10.1016/j.ultsonch.2017.10.001.
- [17] K. Yasui and K. Kato. Bubble dynamics and sonoluminescence from helium or xenon in mercury and water. *Physical Review E—Statistical, Nonlinear, and Soft Matter Physics*, 86(3):036320, 2012. doi: 10.1103/PhysRevE.86.036320.
- [18] K. Kerboua and O. Hamdaoui. Numerical investigation of the effect of dual frequency sonication on stable bubble dynamics. *Ultrasonics Sonochemistry*, 49:325–332, 2018. doi: 10.1016/j.ultsonch.2018.08.025.
- [19] S.S. Rashwan, I. Dincer, and A. Mohany. A unique study on the effect of dissolved gases and bubble temperatures on the ultrasonic hydrogen (sonohydrogen) production. *International Journal of Hydrogen Energy*, 45(41):20808–20819, 2020. doi: 10.1016/j.ijhydene.2020.05.022.
- [20] C. Kalmár, T. Turányi, I.G. Zsély, M. Papp, and F. Hegedűs. The importance of chemical mechanisms in sonochemical modelling. *Ultrasonics Sonochemistry*, 83:105925, 2022. doi: 10.1016/j.ultsonch.2022.105925.
- [21] K. Yasui and K. Kato. Numerical simulations of sonochemical production and oriented aggregation of BaTiO₃ nanocrystals. *Ultrasonics Sonochemistry*, 35:673–680, 2017. doi: 10.1016/j.ultsonch.2016.05.009.
- [22] C.E. Brennen. Cavitation and Bubble Dynamics. Cambridge University Press, 2014. doi: 10.1017/CBO9781107338760.
- [23] Supeno and P. Kruus. Fixation of nitrogen with cavitation. *Ultrasonics Sonochemistry*, 9(1):53–59, 2002. doi: 10.1016/S1350-4177(01)00070-0.
- [24] R. Mettin, C. Cairós, and A. Troia. Sonochemistry and bubble dynamics. *Ultrasonics Sono-chemistry*, 25:24–30, 2015. doi: 10.1016/j.ultsonch.2014.08.015.
- [25] K. Yasuda, T. Torii, K. Yasui, Y. Iida, T. Tuziuti, M. Nakamura, and Y. Asakura. Enhancement of sonochemical reaction of terephthalate ion by superposition of ultrasonic fields of various frequencies. *Ultrasonics Sonochemistry*, 14(6):699–704, 2007. doi: 10.1016/j.ultsonch.2006.12.013.
- [26] K. Yasui, T. Tuziuti, J. Lee, T. Kozuka, A. Towata, and Y. Iida. The range of ambient radius for an active bubble in sonoluminescence and sonochemical reactions. *The Journal of Chemical Physics*, 128(18):184705, 2008. doi: 10.1063/1.2919119.
- [27] K. Yasui. Effect of liquid temperature on sonoluminescence. *Physical Review E*, 64(1):016310, 2001. doi: 10.1103/PhysRevE.64.016310.



[28] K. Kerboua, O. Hamdaoui, M.H. Islam, A. Alghyamah, H.E. Hansen, and B.G. Pollet. Low carbon ultrasonic production of alternate fuel: Operational and mechanistic concerns of the sonochemical process of hydrogen generation under various scenarios. *International Journal of Hydrogen Energy*, 46(53):26770–26787, 2021. doi: 10.1016/j.ijhydene.2021.05.191.

Ferenc KUBICSEK, Ferenc HEGEDŰS, Péter CSIZMADIA

- [29] F. Kubicsek and F. Hegedűs. Assessment of the energy intensity of ammonia production by microbubbles. *Periodica Polytechnica Chemical Engineering*, 69:46–56, 2025. doi: 10.3311/P-Pch.38862.
- [30] F. Kubicsek, Á. Kozák, T. Turányi, I G. Zsély, M. Papp, A. Al-Awamleh, and F. Hegedûs. Ammonia production by microbubbles: A theoretical analysis of achievable energy intensity. *Ultrasonics Sonochemistry*, 106:106876, 2024. doi: 10.1016/j.ultsonch.2024.106876.
- [31] A. Al-Awamleh and F. Hegedűs. Sono-hydrogen: a theoretical investigation of its energy intensity. *Periodica Polytechnica Mechanical Engineering*, 68(3):254–263, 2024. doi: 10.3311/PPme.37299.
- [32] K. Peng, F.G.F. Qin, R. Jiang, W. Qu, and Q. Wang. Production and dispersion of free radicals from transient cavitation bubbles: An integrated numerical scheme and applications. *Ultrasonics Sonochemistry*, 88:106067, 2022. doi: 10.1016/j.ultsonch.2022.106067.
- [33] G.L. Lee and M.C. Law. Numerical modelling of single-bubble acoustic cavitation in water at saturation temperature. *Chemical Engineering Journal*, 430:133051, 2022. doi: 10.1016/j.cej.2021.133051.
- [34] K. Peng, S. Tian, Y. Zhang, Q. He, and Q. Wang. Penetration of hydroxyl radicals in the aqueous phase surrounding a cavitation bubble. *Ultrasonics Sonochemistry*, 91:106235, 2022. doi: 10.1016/j.ultsonch.2022.106235.
- [35] G. Hauke, D. Fuster, and C. Dopazo. Dynamics of a single cavitating and reacting bubble. *Physical Review E—Statistical, Nonlinear, and Soft Matter Physics*, 75(6):066310, 2007. doi: 10.1103/PhysRevE.75.066310.
- [36] B.D. Storey and A.J. Szeri. Water vapour, sonoluminescence and sonochemistry. *Proceedings of the Royal Society of London. Series A: Mathematical, Physical and Engineering Sciences*, 456(1999):1685–1709, 2000. doi: 10.1098/rspa.2000.0582.
- [37] H.Z. Li, Y. Mouline, and N. Midoux. Modelling the bubble formation dynamics in non-newtonian fluids. *Chemical Engineering Science*, 57(3):339–346, 2002. doi: 10.1016/S0009-2509(01)00394-3.
- [38] E. Brujan. Cavitation bubble dynamics in non-Newtonian fluids. *Polymer Engineering & Science*, 49(3):419–431, 2009. doi: 10.1002/pen.21292.
- [39] E. Brujan and P. Williams. Bubble dynamics and cavitation in non-Newtonian liquids. *Rheology Reviews*, pages 147–172, 04 2005.
- [40] E. Brujan. Cavitation in Non-Newtonian Fluids: With Biomedical and Bioengineering Applications. Springer Berlin, Heidelberg, 01 2011. doi: 10.1007/978-3-642-15343-3.
- [41] P. Csizmadia and C. Hős. CFD-based estimation and experiments on the loss coefficient for Bingham and power-law fluids through diffusers and elbows. *Computers & Fluids*, 99:116–123, 2014. doi: 10.1016/j.compfluid.2014.04.004.
- [42] R. Toegel, B. Gompf, R. Pecha, and D. Lohse. Does water vapor prevent upscaling sonoluminescence? *Physical Review Letters*, 85(15):3165, 2000. doi: 10.1103/PhysRevLett.85.3165.
- [43] K. Klapcsik, B. Gyires-Tóth, J.M. Rosselló, and F. Hegedűs. Position control of an acoustic cavitation bubble by reinforcement learning. *Ultrasonics Sonochemistry*, 115:107290, 2025. doi: 10.1016/j.ultsonch.2025.107290.
- [44] K. Klapcsik. Dataset of exponential growth rate values corresponding non-spherical bubble oscillations under dual-frequency acoustic irradiation. *Data in Brief*, 40:107810, 2022. doi: 10.1016/j.dib.2022.107810.



- [45] K. Klapcsik. GPU accelerated numerical investigation of the spherical stability of an acoustic cavitation bubble excited by dual-frequency. *Ultrasonics Sonochemistry*, 77:105684, 2021. doi: 10.1016/j.ultsonch.2021.105684.
- [46] K. Klapcsik and F. Hegedűs. Study of non-spherical bubble oscillations under acoustic irradiation in viscous liquid. *Ultrasonics Sonochemistry*, 54:256–273, 2019. doi: 10.1016/j.ultsonch.2019.01.031.
- [47] P. Kalmár, F. Hegedűs, and K. Klapcsik. A comparative study of measurements and numerical simulations of acoustically excited non-spherical bubbles oscillation. *International Journal of Multiphase Flow*, 179:104947, 2024. doi: 10.1016/j.ijmultiphaseflow.2024.104947.
- [48] S.J. Shaw. Translation and oscillation of a bubble under axisymmetric deformation. *Physics of Fluids*, 18(7), 2006. doi: 10.1063/1.2227047.
- [49] S.J. Shaw. The stability of a bubble in a weakly viscous liquid subject to an acoustic traveling wave. *Physics of Fluids*, 21(2), 2009. doi: 10.1063/1.3076932.
- [50] O. Louisnard and F. Gomez. Growth by rectified diffusion of strongly acoustically forced gas bubbles in nearly saturated liquids. *Physical Review E*, 67(3):036610, 2003. doi: 10.1103/Phys-RevE.67.036610.
- [51] J. Otomo, M. Koshi, T. Mitsumori, H. Iwasaki, and K. Yamada. Chemical kinetic modeling of ammonia oxidation with improved reaction mechanism for ammonia/air and ammonia/hydrogen/air combustion. *International Journal of Hydrogen Energy*, 43(5):3004–3014, 2018. doi: 10.1016/j.ijhydene.2017.12.066.
- [52] F. Kubicsek. Mechanism file of the Otomo2018 reaction mechanism. URL: https://github.com/kozakaron/Bubble_dynamics_simulation/blob/mrkf100-nonnewtonian/ reaction_mechanism_Otomo_ammonia.pdf, accessed 14 June 2025.
- [53] Y. Song, H. Hashemi, J.M. Christensen, C. Zou, P. Marshall, and P. Glarborg. Ammonia oxidation at high pressure and intermediate temperatures. *Fuel*, 181:358–365, 2016. doi: 10.1016/j.fuel.2016.04.100.
- [54] W. Tsang and R.F. Hampson. Chemical kinetic data base for combustion chemistry. Part I. Methane and related compounds. *Journal of Physical and Chemical Reference Data*, 15(3):1087–1279, 1986. doi: 10.1063/1.555759.
- [55] T. Turányi and A.S. Tomlin. Analysis of Kinetic Reaction Mechanisms, volume 20. Springer, 2014. doi: 10.1007/978-3-662-44562-4.
- [56] F. Hegedűs, C. Kalmár, T. Turányi, I.G. Zsély, and M. Papp. Sonochemical reactions, when, where and how: Modelling approach. In *Energy Aspects of Acoustic Cavitation and Sonochemistry*, pages 49–77. Elsevier, 2022. doi: 10.1016/B978-0-323-91937-1.00013-X.
- [57] M.T. Warnez and E. Johnsen. Numerical modeling of bubble dynamics in viscoelastic media with relaxation. *Physics of Fluids*, 27(6), 2015. doi: 10.1063/1.4922598.
- [58] Á. Kozák. Bubble dynamics simulation, 2023. URL: https://github.com/kozakaron/Bubble_dynamics_simulation/tree/mrkf100-nonnewtonian, accessed 10 April 2025.
- [59] A.J. Sojahrood, H. Haghi, R. Karshafian, and M.C. Kolios. Nonlinear model of acoustical attenuation and speed of sound in a bubbly medium. In 2015 IEEE International Ultrasonics Symposium (IUS), pages 1–4, Taipei, Taiwan, 2015. doi: 10.1109/ULTSYM.2015.0086.
- [60] I. Rafiqul, C. Weber, B. Lehmann, and A. Voss. Energy efficiency improvements in ammonia production—perspectives and uncertainties. *Energy*, 30(13):2487–2504, 2005. doi: 10.1016/j.energy.2004.12.004.
- [61] F. Kubicsek. Analysis of the chemical yield of sonochemical reactors, TDK Thesis, Budapest University of Technology and Economics (in Hungarian), 2021. URL: https://tdk.bme.hu/ConferenceFiles/GPK/2021/Paper/Szonokemiai-reaktor-kemiai-kihozatalanak. pdf?paperId=10808, accessed: 14 June 2025.